Biodegradable Nanoneedles for Localized Delivery of Nanoparticles *in Vivo:* Exploring the Biointerface

Ciro Chiappini,[†] Jonathan O. Martinez,[‡] Enrica De Rosa,[‡] Carina S. Almeida,[†] Ennio Tasciotti,[*,‡] and Molly M. Stevens[*,†,§,∥]

[†]Department of Materials, [§]Department of Bioengineering, and [∥]Institute of Biomedical Engineering, Imperial College London, London, SW7 2AZ, U.K. and [‡]Department of Nanomedicine, Houston Methodist Research Institute, Houston, Texas 77030, United States

ABSTRACT Nanoneedles display potential in mediating the delivery of drugs and biologicals, as well as intracellular sensing and single-cell stimulation, through direct access to the cell cytoplasm. Nanoneedles enable cytosolic delivery, negotiating the cell membrane and the endolysosomal system, thus overcoming these major obstacles to the efficacy of nanotherapeutics. The low toxicity and minimal invasiveness of nanoneedles have a potential for the sustained nonimmunogenic delivery of payloads *in vivo,* provided that the development of biocompatible nanoneedles with a simple deployment strategy is achieved. Here we present a mesoporous silicon nanoneedle array that achieves a tight interface with the cell, rapidly negotiating local biological barriers to grant temporary access to the cytosol with minimal impact on cell viability. The tightness of this interfacing enables both delivery of cell-impermeant quantum dots *in vivo* and live intracellular sensing of pH. Dissecting the biointerface over time elucidated the dynamics of cell association and nanoneedle biodegradation, showing rapid interfacing leading to cytosolic payload delivery within less than 30 minutes *in vitro*. The rapid and simple application of nanoneedles *in vivo* to the surface of tissues with different architectures invariably resulted in the localized delivery of quantum dots to the superficial cells and their prolonged retention. This investigation provides an understanding of the dynamics of nanoneedles' biointerface and delivery, outlining a strategy for highly local intracellular delivery of nanoparticles and cell-impermeant payloads within live tissues.

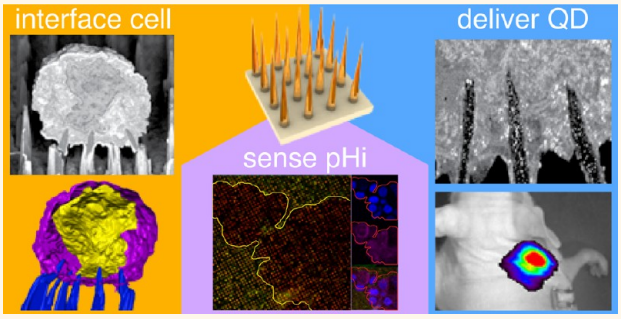

KEYWORDS: nanoneedles · porous silicon · drug delivery · nanomedicine · biointerface · pH sensing · quantum dots

Vertical arrays of nanoneedles can provide access to the cell cytosol and interact with the intracellular environment without eliciting toxicity or altering cell metabolism.[1−4] Recent advances have indicated that nanoneedles may outperform currently available technology for the delivery of nucleic acids[3,5,6] and for the intracellular recording and stimulation of excitable cells.[7] However, the widely employed interfacing (*i.e.*, nanoinjection) strategies, while suitable for nanoinjection in culture, possess limited translational potential *in vivo*.[4,7−9] Nanoinjection requires cell activity,[10,11] centrifugation,[12] AFM operation,[13] or electroporation[14] in order to guarantee intracellular interaction. Cell activity is highly dependent on cell type and its environment and requires prolonged interfacing;[1] electroporation is accompanied by high cytotoxicity and immune response,[15,16] while centrifugation and AFM operation are applicable only to cultures.

Semiconducting nanowires[3,17] and carbon nanofibers/nanotubes[4,18] constituting the vast majority of nanoneedles are not biodegradable and have demonstrated poor *in vivo* biocompatibility. Carbon nanowires can exhibit high cytotoxicity by multiple exposure routes and targeting different organs,[19,20] leading to diverse pathologies including acute inflammation,[21] foreign body response,[22] and cancer.[23] These effects can be mitigated during synthesis[22,23] or before deployment,[24] but safety concerns remain, especially when envisioning a minimally invasive, nonimmunogenic treatment. Silicon is a poor biomaterial eliciting thrombus formation in contact with blood[25,26] and foreign body response

* Address correspondence to etasciotti@houstonmethodist.org, m.stevens@imperial.ac.uk.

Received for review March 9, 2015 and accepted April 10, 2015.

Published online April 10, 2015
10.1021/acsnano.5b01490

subcutaneously.[27] On the other hand porous silicon (pSi) is a viable candidate for the fabrication of biocompatible nanoneedles. It is a biodegradable[28] and highly biocompatible material,[29] employed *in vivo* for ocular implants[30] and as a drug delivery vector particulate for intravenous injection[8,31,32] and was tested in humans as a brachytherapy device.[33] Porous silicon nano- and microparticle uptake studies in culture have demonstrated elevated cytocompatibility following internalization.[31] Intravenously delivered pSi *in vivo* can distribute across all organs in the body[8,34] and be cleared within a few weeks,[8] without causing adverse reactions or eliciting inflammation.[32,35] Indeed pSi use in humans has been evaluated as safe and risk-free in phase I and phase II clinical trials.[33,36]

Further development of nanoneedle technologies requires a more critical comprehension of the process of nanoinjection in both isolated cells and whole tissues to improve the design and engineer nanoneedles with optimal nanoinjection potential. Still very little is known regarding the dynamics and localization of nanoneedles and their payload upon interfacing with cells. The very penetration of nanoneedles across the cell membrane is hotly debated.[1,3,37,38]

A growing body of evidence indicates that *in vitro* nanoinjection enables the crossing of the membrane barrier and allows for the direct colocalization with intracellular organelles and cytosolic structures.[1−3,5,13] The sudden drop in force that occurs when applying a nanoneedle has been interpreted as the crossing of a physical barrier, the cellular membrane.[13] Confocal microscopy reveals that nanoneedles are often colocalized with the cytosol or nucleus.[3] In addition, nanoneedles can effectively deliver labile biological therapeutic agents in their active form to the nucleus and/or the cytosol, confirming their ability to efficiently reach the intracellular space.[1,3] The buildup of large forces at the interface between the cell membrane and the high aspect ratio needle structure has recently been proposed as the mechanism leading to self-puncturing and cytosolic display,[39] with self-puncturing being directly observed in mammalian cells.[10]

Conflicting evidence suggests that nanoneedles may simply be tightly associated with the cell membrane, but not cross it completely. For example, the perinuclear fluorescent signal often associated with nanoneedle-mediated delivery implies that a large portion of the payload was internalized through a classic endocytic pathway.[3] Furthermore, sensing of intracellular electrical activity in several instances requires the initial application of a voltage pulse, to first induce membrane poration.[37] Electron microscopy imaging of *in vitro* nanoinjection reveals that short nanopillars of solid silicon appear unable to cross the plasmalemma.[38] Longer thinner nanowires instead can significantly invaginate the plasma membrane[40,41] or be internalized by the endolysosomal system as isolated broken fragments.[42] Little is known about the impact and cytotoxicity of nanoneedles inserted within cells and tissues; however cells grown over nanoneedles present unaltered respiratory metabolism, membrane integrity, proliferation, and housekeeping gene expression.[1]

Nanoinjection has the unique potential to deliver nanoparticles to a specific set of cells in a localized region, without involving the vast majority of the tissue. The study reported here employs our recently developed class of porous silicon nanoneedles[6] to investigate their biointerface and the cytosolic delivery of nanoparticles. These porous silicon nanoneedles negotiate the endolysosomal system, allowing the sensing of intracellular pH without inducing apoptosis. Dissecting the kinetics of the nanoneedles' interface and of quantum dots delivery yields insight into their cytosolic interaction and any nuclear envelope remodeling. The kinetic study also highlights the similarities and differences in interfacing and delivery existing between forceful nanoinjection compared to the seeding of cells over nanoneedles. Finally nanoinjection in mice demonstrates localized delivery of nanoparticles to the superficial layers of architecturally different mammalian tissues. The evolution of the nanoneedle biointerface and the dynamics of payload delivery are studied, and the nanoneedles are applied as a system for the localized two-dimensional delivery of nanoparticles to the cell in live tissues of widely different architectures.

RESULTS

Porous Silicon Nanoneedles. The synthesis of pSi nanoneedle arrays (nanoneedles) combined microfabrication with metal assisted chemical etching. The needles were arranged in a square lattice with 2 μm pitch, were 5−7 μm tall, and had a tip diameter of <50 nm, a 600 nm base, and 50% porosity with a 10−15 nm pore size (Figure 1a). A single process yielded a 100 mm wafer uniformly covered with needles. Photolithography followed by reactive ion etching defined the desired pattern on a thin film of low-stress nitride over the silicon substrate (Figure 1b). Electroless deposition formed dendritic Ag nanoparticles selectively on the exposed silicon between the patterned areas. Metal-assisted chemical etching of this substrate[43] yielded pSi pillars, which reactive ion etching shaped into conical nanoneedles. This high-throughput and parallelized fabrication strategy did not require direct writing and granted control over the geometry, arrangement, and nanoscale porosity of the needles.

In pursuing optimal biocompatibility and interfacing, our design choices were informed by the available literature and by our experience with pSi nanomaterials. A smaller tip diameter provides a tighter cell−needle interface[38] and favors the delivery of drugs across the cell membranes while reducing

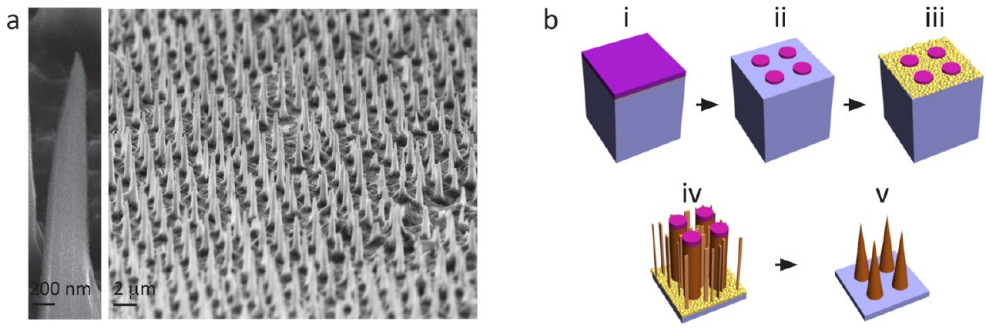

Figure 1. Porous silicon nanoneedles and their fabrication process. (a) Scanning electron micrographs of a uniform array of conical pSi nanoneedles, with a <100 nm tip diameter, 600 nm base diameter, 5 μm length, and 2 μm pitch. (b) Schematic diagram of the nanoneedle fabrication process. (i) Deposition of a low-stress silicon nitride thin film by low-pressure chemical vapor deposition. (ii) Patterning of 600 nm silicon nitride disks. (iii) Selective deposition of Ag dendrites over the exposed silicon by electroless deposition from $AgNO_3$ salts. (iv) Metal assisted chemical etching in oxidizing solution of HF to obtain pSi pillars interspersed with pSi nanowires. (v) Reactive ion etching in SF_6 plasma to shape pillars into conical nanoneedles and remove nanowires.

cytotoxicity.[1,9,13] Our previous investigations of pSi microparticles for systemic drug delivery indicated that a 10 nm pore size enabled optimal loading of hydrophilic quantum dots with a 6 nm diameter,[44] while the 50% porosity provided a 600-fold increase in surface area over solid structures and allowed full degradation within a day.[45]

Nanoinjection Provides Safe Intracellular Interfacing and Delivery. Nanojection was performed either by seeding cells over an array of nanoneedles (nanoneedles on bottom, nN-B) or by forcibly applying the nanoneedles from the top of the cell monolayer (nanoneedles on top, nN-T). Forcible application employed a centripetal acceleration of 100 rcf on a 70 mg chip, leading to an effective force of 68 mN shared across the 1.6×10^7 nanoneedles present on the chip, effectively applying a theoretical load of 4.25 nN per needle. This force is compatible with nanoneedle intracellular penetration, being higher than the threshold identified for a nanoneedle to cross a plasma membrane (0.5 to 2 nN).[9] We have previously observed that nanoinjection does not affect viability or proliferation of cells.[6]

A pH sensor was built by covalent attachment of a pH-sensitive fluorophore (fluorescein isothiocyanite, FITC) and a reference fluorophore (AlexaFluor 633, AF633) to the nanoneedles. The response of this sensor to pH was measured by ratiometric fluorescence and was found to be linear in the biologically relevant range of pH (6.1 to 7.9, Figure S1). Upon nanoinjection *in vitro*, this sensor mapped intracellular pH (pHi) with single-cell resolution alongside extracellular pH (pHe). The OE33 esophageal adenocarcinoma cell line displayed significant quenching of FITC fluorescence in correspondence with most nanoneedles underlying cells, corresponding to a ratiometric measurement of pH 6.7 (Figure 2a,c,d). Conversely the nanoneedles tested with Het-1A cells displayed a ratiometric fluorescence equivalent to pH 7.2 (Figure 2b,c,d). Both findings were in agreement with the pHi measured for OE33 (cancer cells) and Het-1A (healthy cells) by 2′,7′-Bis-(2-Carboxyethyl)-5-(and-6)-Carboxyfluorescein (BCECF) ratiometric fluorescence assay (Figure S2). The pH 7.4 measured for free-standing nanoneedles was consistent with the pHe of the culture medium (Figure 2c,d). In OE33 cultures, a red nanoneedle would be sensing a pH equivalent to pHi, while a yellow-green one would be sensing pHe. Upon nanoinjection, the vast majority of nanoneedles underlying OE33 cells sensed pHi (Figure 2a).

Loading a fluorescent payload within the mesoporous network of the pH-sensing nanoneedles enabled combined intracellular sensing and delivery. The vast majority of cells in culture displayed cytosolic localization of the fluorescent payload (Figure 2e). All cells displaying cytosolic fluorescence were also underpinned by nanoneedles sensing pHi. The intracellular delivery and sensing appeared to have a minimal impact on cell viability, as evidenced by the few apoptotic cells in Figure 2e (green nuclei indicated by blue arrows).

Exploring the Cell−Nanoneedle Interface. Following nanoinjection, confocal microscopy revealed intact nanoneedles interfaced to the cytosol of cells. Several nanoneedles colocalized with the nuclear region regardless of injection strategy (Figure 3a−e). In agreement with the pHi measurements, confocal microscopy suggested a tight cytosol−nanoneedle interface, showing nanoneedles several hundreds of nanometers above the red membrane staining, but could not provide detailed information regarding their interaction with subcellular structures (*i.e.*, cytoskeleton, vesicles, *etc.*) or their mutual positioning with respect to the nucleus.

To visualize the cell−nanoneedle interface at higher resolution, we processed the cells using a slice-through imaging approach combined with dual-beam focused ion beam−scanning electron microscopy (FIB-SEM) (Figure 3b,e, Movies S1−S8). In agreement with the nanoneedles' ability to sense pHi, FIB-SEM suggested that nanoneedles tightly interfaced with the cytosol (Figure 3b,e, Figure S3). Several nanoneedles seemed to be pinned to the nucleus, with the nuclear

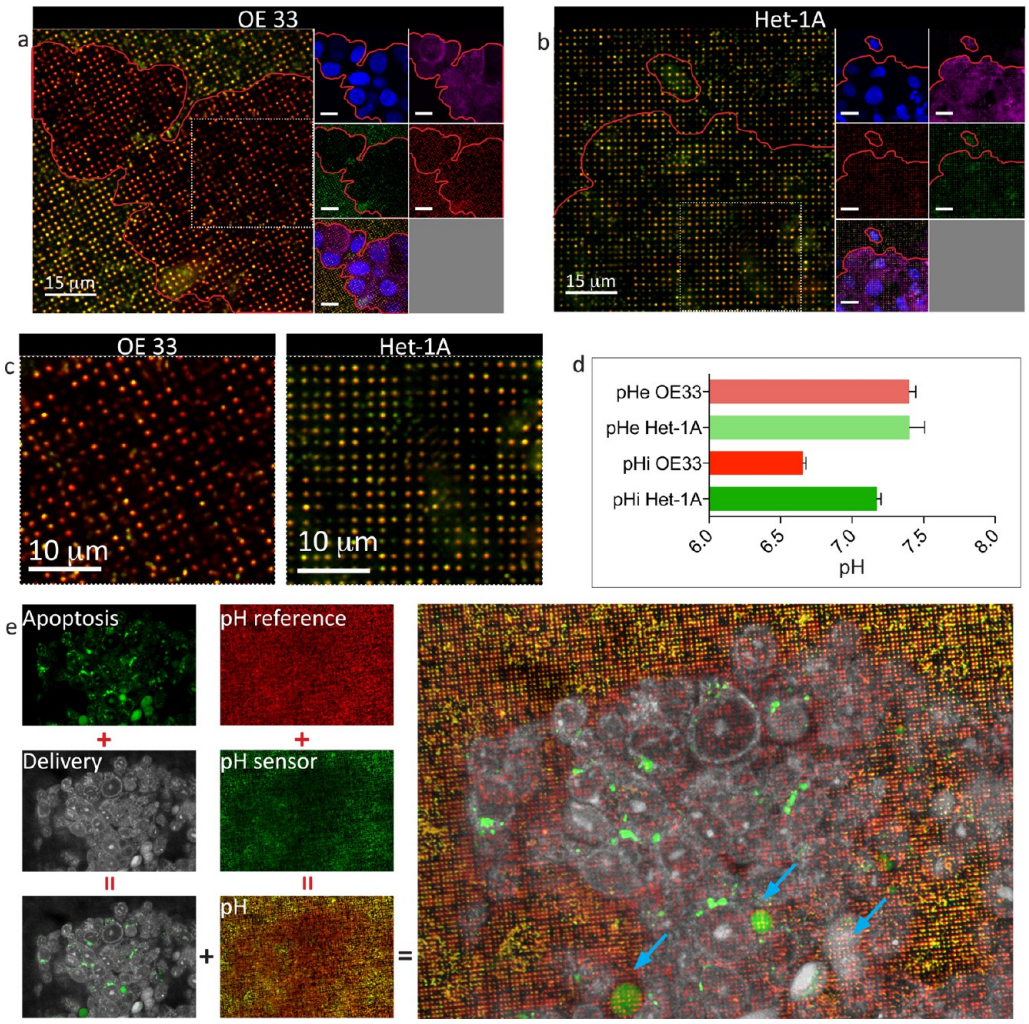

Figure 2. Nanoneedles mediate simultaneous intracellular pH sensing and delivery to viable cells. (a, b) Nanoneedles simultaneously functionalized with FITC (green) and AF633 (red) sense intracellular and extracellular pH for OE33 (a) and Het-1A (b) cells (nucleus in blue, membrane in magenta) in culture. (c) Magnifications of the outlined insets from panels (a) and (b) showing the different optical readout for OE33 and Het-1a cells. (d) Quantification of intracellular and extracellular pH as measured by nanoneedles. (e) Caspase 3/7 activity assay in conjunction with intracellular pH measurement and delivery by confocal microscopy. The confocal micrograph shows limited nuclear localization of caspase 3/7 (first panel, nuclear green stain; blue arrows, main panel), universal cytosolic delivery to cells (white), and sensing of lower intracellular pH (red nanoneedles) compared to extracellular (yellow nanoneedles) in OE33 cells. The green and white micrographs for the delivery and caspase activity are acquired at the same *z*-plane above the nanoneedles; the red and green micrographs for pH measurements are acquired at the same *z*-plane within the nanoneedles.

envelope being remodeled to wrap around each nanoneedle (Figure S4, Movies S3, S7). Importantly, the needles localizing within the non-nuclear areas of the cell never appeared to emerge from the far side of the cell (Figures S3, S5, Movies S1−S3, S5−S7). Regardless of the nanoinjection strategy (nN-B or nN-T), cells exhibited flexible nuclear and plasma membrane rearrangements in response to the puncturing needle.

Confocal microscopy and SEM-FIB analysis showed that as early as 1 h after seeding, the tip of the nanoneedles appeared to interface with the cytosol and in close proximity to the nucleus (Figure 3d−i, Figure S6a, Movie S1). Quantification of segmented SEM-FIB images confirmed that the needles progressively increased their interfacing with the cytosol while reducing their distance to the nucleus (Figure 3h,i). After 8 h the nanoneedles interfaced with the cytosol for a depth of 2 μm and appeared to have contacted the nuclear envelope, inducing nuclear remodeling (Figure 3e,g−i, Movies S1−S8). Immediately after seeding, cells retained the typical spherical shape of the early stages of cell spreading (Figure 3d−g, Movies S1, S2). At later time points, the cells continued to extend and spread, wrapping the tips of their filopodia around the neighboring needles (Figure S6).

Throughout the process of interfacing the nanoneedles experienced progressive degradation, effectively increasing their porosity and reducing their mechanical stability. Inspection of the nanoneedles 8 h after injection revealed they retained their morphology. After 15 h, nanoneedles were visibly degraded (Figure S7) until only the solid stump of the

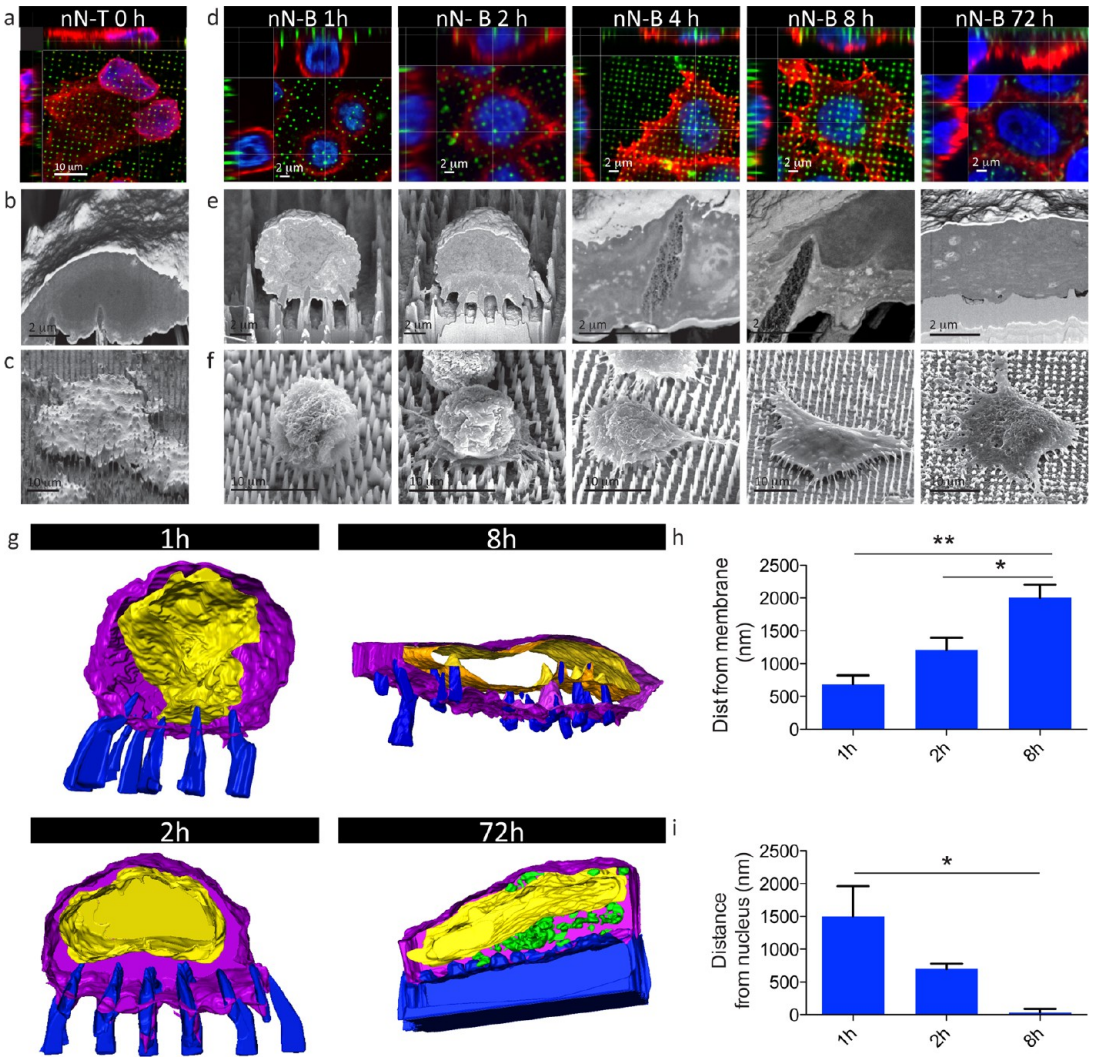

Figure 3. Cell−nanoneedle interface upon nanoinjection. (a−c) nN-T nanoinjection showing cytosolic interfacing and exclusion from the nucleus 1 min following nanoinjection. (d−f) Temporal evolution of nN-B nanoinjection showing progressive cytosolic interfacing and nuclear exclusion with associated remodeling of the nuclear envelope. (a, d) Laser scanning confocal micrographs at the time points indicated. Cell membrane is in red, nuclei are in blue, and nanoneedles are in green. (b, e) FIB-SEM cross sections of nanoinjected cells. (c, f) 54° tilt SEM micrographs showing retained cell morphology. (g) Three-dimensional reconstruction FIB-SEM slice through segmentation at different times for nN-B nanoinjection. Nanoneedles are in blue, cell membrane is in purple, nuclear envelope is in yellow, and electron dense areas attributed to Si are in green (72 h). (h) Quantification of the nanoneedle depth of cytosolic interfacing, measured as the distance between the tip of the nanoneedle and the underlying cell membrane. (i) Quantification of the distance of nanoneedles from the nucleus, measured as the distance between the tip of a nanoneedle and the cell nucleus. *$p < 0.05$, **$p < 0.01$.

needles remained by 72 h. At this time no recognizable nanostructure resembling the nanoneedles could be found within the cells (Figure 3d−g, Figure S8, Movies S4, S8). The electron dense regions observed in the cytosol likely represent areas of high Si concentration that arose from the degradation of the nanoneedles (Figure 3e,g, Movies S4, S8). Similarly, the confocal micrographs of nanoneedles covalently tagged with a fluorescent dye displayed intracellular regions of green fluorescence, likely originating from the dye initially conjugated to the needles (Figure 3d).

Cytosolic Nanoinjection of Quantum Dots. Fluorescent 6 nm hydrophilic quantum dots were loaded in the porous structure of the nanoneedles (Figure S9a) and nanoinjected into cells. Confocal microscopy confirmed that quantum dots diffused rapidly throughout the cytosol of all cells (Figure 4a,b). SEM-FIB confirmed that quantum dots localized both on the nanoneedles and within the cytosol of nanoinjected cells, but not within the nucleus (Figure 4c, Figure S10). Transmission electron microscopy coupled with elemental analysis validated the intracellular presence of quantum dots and their free accumulation in the cytosol outside of the membranous organelles constituting the endolysosomal system (Figure 4d, Figure S11).

The same amount of quantum dots delivered in solution could not be detected intracellularly by SEM-FIB and generated limited fluorescence associated with the cell body (Figure 4a,c), thus confirming that

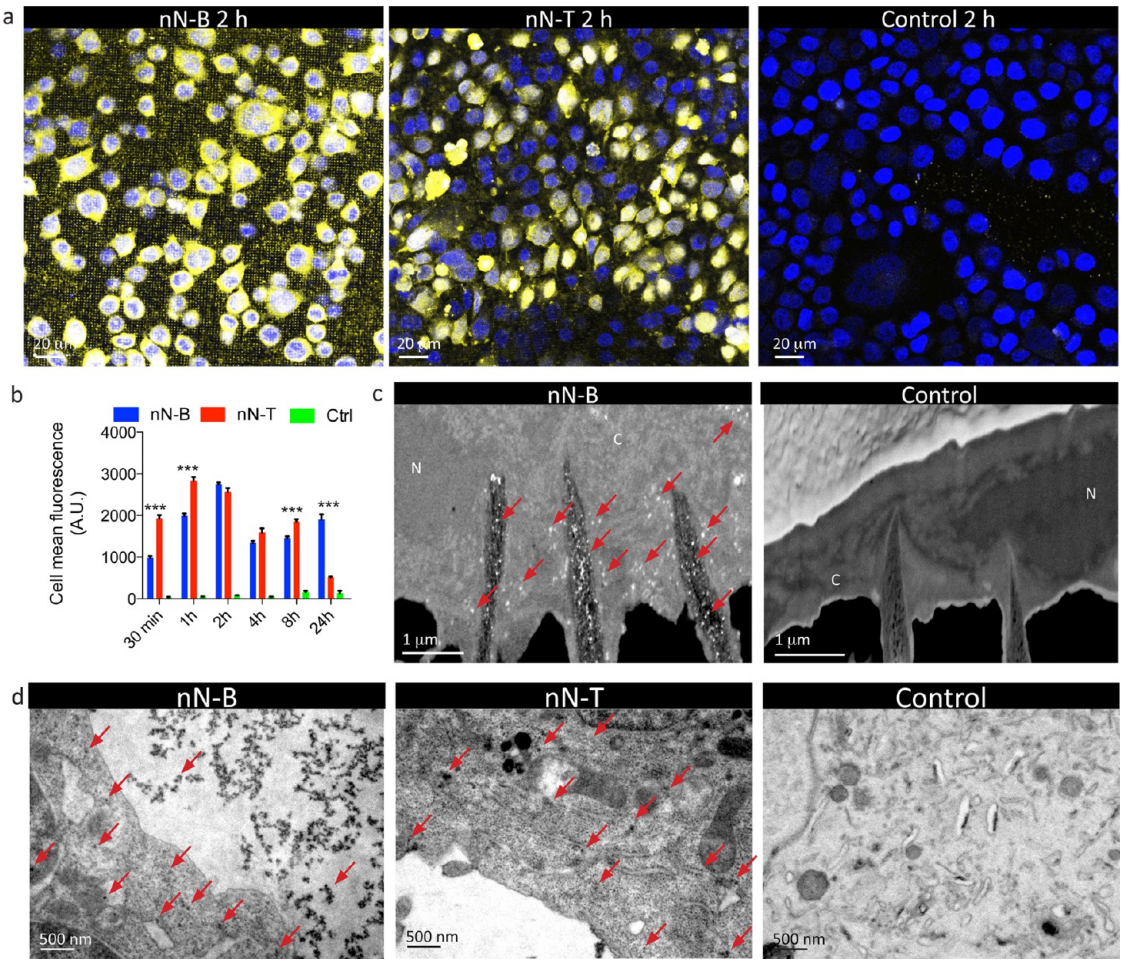

Figure 4. Nanoinjection of quantum dots. (a) Confocal micrograph of cells nanoinjected with 570 nm emission quantum dots at 2 h following interfacing. Control represents cells grown on nanoneedles with quantum dots added in solution. Cell nuclei are in blue; quantum dots in yellow. (b) Quantification of quantum dots released within cells as a function of time for the three delivery strategies depicted in panel (a). ***$p < 0.001$ for nN-B *vs* nN-T. (c) FIB-SEM cross sections of cells nanoinjected with quantum dots (nN-B) and empty nanoneedles with quantum dots in solution (control). The loaded nanoneedles deliver quantum dots to the cytosol (indicated by red arrows). N indicates the nucleus, and C the cytosol. (d) TEM micrographs of ultrathin (90 nm) sections of cells nanoinjected with quantum dots (nN-B, nN-T) and empty nanoneedles with quantum dots in solution (control). Red arrows indicate some of the larger aggregates of quantum dots.

the delivery of quantum dots was directly mediated by the nanoneedles. Both nN-B and nN-T showed cytosolic accumulation of quantum dots as early as 30 min following nanoinjection (Figure 4b) and reached a plateau within 1 h. nN-B samples retained 69% of the payload at 24 h, compared to 18% of nN-T (Figure 4a,b). The delivery of quantum dots occurred more rapidly for nN-T, likely due to the earlier, deeper interfacing of the nN-T nanoinjection, which at 1 min displayed a similar profile to nN-B at 8 h (Figure 2). While the average peak delivery was similar for the two approaches, nN-B delivery was more uniform across cells, especially at shorter times (Figure 4a,b). While the nN-T cells were adherent on the substrate for at least 24 h prior to nanoinjection, the nN-B cells needed additional time to initially adhere and spread to the nanoneedles. In agreement with our prior observations during the exploration of the cell–nanoneedle interface, these results may reflect the more uniform and gradual interaction with the cytosol for the nN-B (Figure 4a,b).

Bovine serum albumin (BSA) and siRNA were simultaneously loaded into nanoneedles, showing uniform distribution throughout the entire porous matrix (Figure S9b–d). In both nanoinjection strategies the BSA and siRNA payloads were delivered to the cytosol similarly to what was observed with quantum dots (Figure S12).

Nanoinjection of Quatntum Dots to Muscle and Skin. *In vivo* nanoinjection of quantum dots to an exposed muscle and two skin locations allowed evaluation of localized nanoparticle delivery in mice. Regardless of the tissue, quantum dots were confined to a limited volume associated with the surface layer contiguous to the site of nanoinjection (Figure 5a,b Figure S13). Quantum dot fluorescence was observed originating from the cytosolic region of cells located at the surface (Figure 5a), and TEM confirmed the presence of quantum dots associated with cells (Figure 5c).

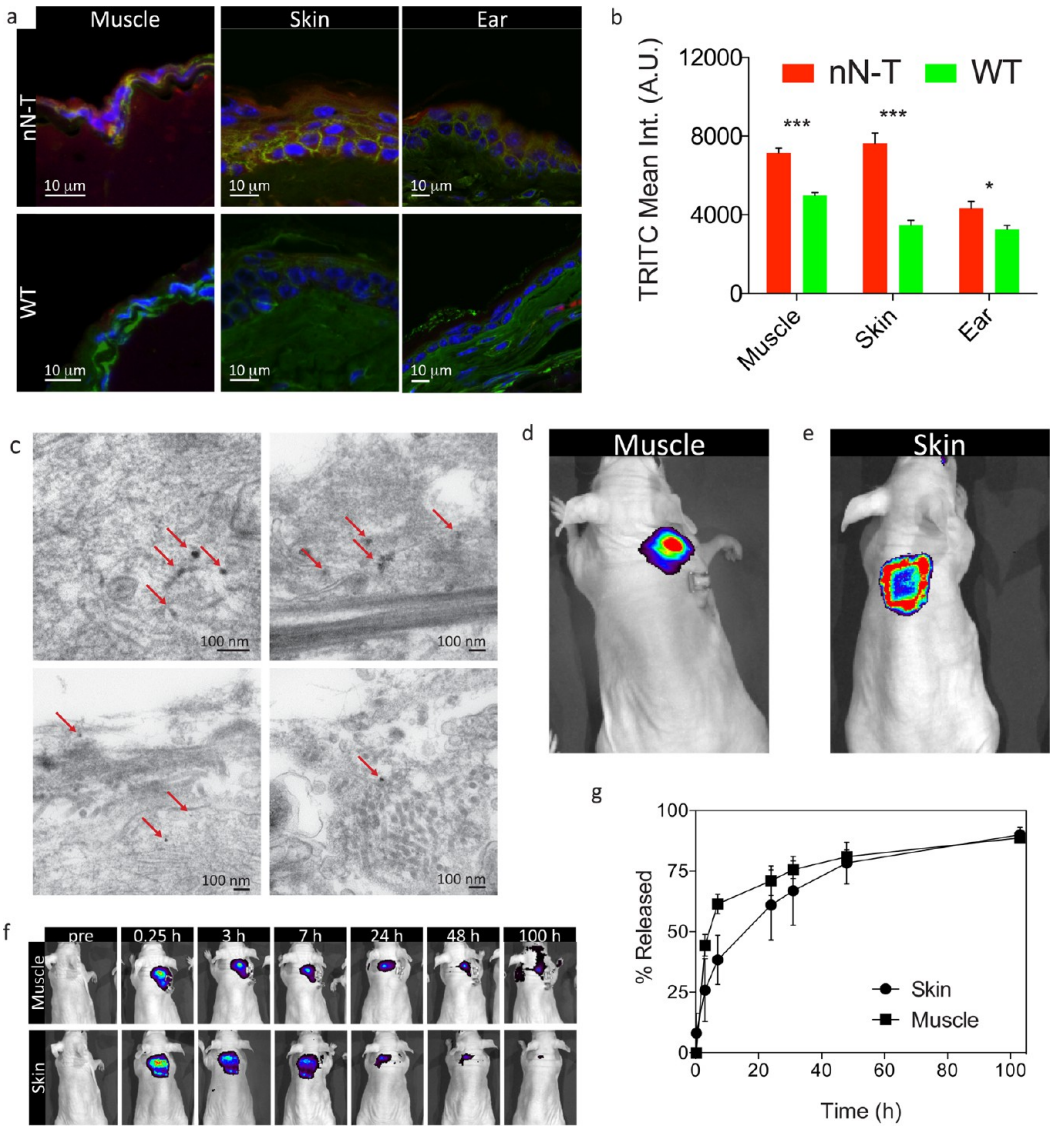

Figure 5. ***In vivo*** **delivery of quantum dots by nN-T. (a) Immunofluorescence histology of the cross section of tissues nanoinjected with quantum dots compared to untreated tissue. Quantum dots are in red, cell membrane is in green, and cell nuclei are in blue. (b) Quantification of quantum dots delivery through fluorescence of histological cross sections such as the ones depicted in Figure S10. All tissues show a significant increase in fluorescence upon nanoinjection. ***$p < 0.001$, *$p < 0.05$. (c) Transmission electron micrograph of the cross section of the muscle tissue treated with nanoneedles. Red arrows indicate quantum dot accumulations. (d, e) Fluorescent live imaging of the muscle (d) and skin (e) nanoinjection sites. (f) Longitudinal live animal fluorescent imaging of the nanoinjection site for muscle and skin, showing prolonged retention of the quantum dots at the delivery site for up to 100 h. (g) Quantification of the fluorescent imaging showing the amount of dye that is dispersed away from the delivery site as a function of time.**

In skin and muscle, nanoinjection left a square fluorescent mark at the delivery site, which replicated the geometry of the nanoneedle chip (Figure 5d–f). Further confirming delivery within the tissue, nanoinjected quantum dots were retained for up to 100 h around the injection site (Figure 5f). By comparison, quantum dots delivered through a flat silicon chip completely dispersed in less than 24 h (Figure S14).

DISCUSSION

Porous silicon nanoneedles can efficiently load a nanoparticle payload and direct its delivery to the cells in a localized superficial area of tissue. The nanoneedles' ability to sense intracellular pH and direct cytosolic delivery of different payloads (nanoparticles, dyes, proteins, nucleic acids) combined with the limited occurrence of apoptosis support the available literature to indicate the efficacy, minimal invasiveness, and safety potential of nanoinjection.

Nanoinjection of quantum dots to the cell cytosol occurred rapidly after interfacing with the cell. The nN-B nanoinjection relied on active cell processes for minimally disruptive intracellular delivery. Conversely nN-T proved to be a viable option for nanoinjection *in vivo*, as it delivered the payload to the cells' cytosol through a rapid and forcible interfacing. During

nanoinjection the needles progressively interfaced with the cytosol while the cell nucleus remodeled to minimize or avoid interfacing. This display of active cellular movement subsequent to needle penetration was a further confirmation of the low impact of nanoneedles on cell metabolism.

The superficial intracellular delivery observed *in vivo* was extremely localized to the area interfaced by the needles and did not reach the bulk of tissues or cross tissue barriers such as the stratum corneum of the skin. The local nature of the interaction suggests that nanoneedles-mediated delivery or sensing would occur only at the immediate region of interfacing, with minimal involvement of the remaining tissue.

Microneedles typically require a high insertion velocity to deliver a payload *in vivo*.[46] Conversely our nanoinjection strategy has very low impact on the tissues while showing prolonged retention of the payload at the delivery site. The minimally invasive, uniform, and controlled access to the cytosol of a large number of cells within a defined or patterned area, combined with the ability to deliver to and sense the intracellular space with the potential to discriminate cancer (OE33) from healthy (Het-1A) cellular microenvironment, can pave the way toward nanoscale interaction and interrogation of cells within complex architectures for the assessment of tissue pathologies at the single-cell level.

METHODS

An expanded methods section covering the details of all methods employed in this study is available as Supporting Information.

Nanoneedles Fabrication. A layer of 160 nm of low-pressure chemical vapor deposition low-stress silicon nitride was deposited on boron-doped p-type, 100 mm, 0.01 Ω-cm Si wafers. The photolithographic pattern consisting of 600 nm diameter disks with a 2 μm pitch was transferred on the photoresist-coated substrate. Pattern transfer limited to the silicon nitride layer was performed by CF_4 reactive ion etching. The photoresist was then stripped.

Electroless deposition of Ag on the patterned Si wafer occurred in an HF solution of 0.02 M $AgNO_3$ 20 mL of 49% wt HF, and 75 mL of H_2O, following substrate cleaning in 10% wt HF. The substrate was rinsed and dried. Metal-assisted chemical etch occurred in 80 mL of 49% wt HF, 316 mL of H_2O, and 4 mL of H_2O_2 for 8 min 30 s followed by reactive ion etch in SF_6 plasma. The substrate was then diced into 8 × 8 mm chips and oxidized by O_2 plasma.

Nanoneedles on Bottom Interfacing *in Vitro* (nN-B). The sterilized chip carrying the nanoneedles (70% v/v ethanol in deionized water, 1 h) was dried and UV irradiated for 1 h. The chip was placed at the bottom of a 24-well plate and rinsed three times with PBS. The desired density of cells (typically around 1×10^5 cells) was seeded over the needles, and the well plate was returned to the incubator.

Nanoneedles on Top Interfacing *in Vitro* (nN-T). Cells were seeded in a 24-well plate at 5×10^4 cells/well and incubated for 24−48 h until reaching >60% confluence. The cell culture medium was exchanged with 2 mL of fresh medium, and the nanoneedle chip was immersed in the medium face down. The plate was transferred to a swinging bucket centrifuge with appropriate counterweight and spun at 100 rcf for 1 min. If the experiment required incubation for longer than 30 min, the chips were flipped face up at 30 min.

Quantum Dots Delivery. Nanoneedles loaded with quantum dots were interfaced with HeLa cells, either nN-T or nN-B. The control samples were interfaced nN-B, and the same volume of quantum dots as for the nanoneedles was added to the medium together with the cells. At each time point the samples were washed five times in PBS and then fixed in 4% v/v paraformaldehyde in PBS for 15 min at RT. The samples were further washed in PBS, stained with DAPI, and finally mounted on coverslips. A single *z*-slice immediately above the nanoneedle tips was acquired for each sample on a Leica SP5 inverted laser scanning confocal microscope, and the area normalized fluorescence intensity of 50 cells for each of three images was evaluated using Volocity (PerkinElmer, USA). Three randomly acquired images per sample were analyzed. Experiments were performed in triplicate, and data are reported as the mean with standard error of the mean.

Combined pH Sensing, Fluorophore Delivery, and Caspase Activity Monitoring. Nanoneedles were functionalized for pH sensing and delivery (Supporting Information). Cells were nN-T nanoinjected and allowed to equilibrate for 30 min in an incubator. The medium was then completely replaced adding the caspase 3/7 detection assay in fresh HEPES buffered DMEM without phenol red or other supplementation. The assay was incubated for 30 min in a cell culture incubator. In this assay, caspase activity cleaves a substrate, allowing it to bind the nuclear DNA and enhance its fluorescence. Caspase activity is characterized by intense green nuclear fluorescence.

Cells were then imaged by confocal microscopy. A single *z*-plane was imaged for the FITC emission and the AF 633 emission, maintaining laser power, photomultiplier gain, and wavelength acquisition window constant across all samples. Caspase activity and fluorophore delivery were imaged in a different *z*-plane than the pH, this z-plane lying above the tip of the nanoneedles.

The pH images were analyzed in a custom Matlab program that identified the nanoneedles from the background, calculated the fluorescence emission ratio of FITC/AF633 singularly for each nanoneedle, and then averaged it over a preselected region of interest.

Nanoneedles on Top Interfacing *in Vivo*. Animal studies were performed in accordance with the guidelines of the Animal Welfare Act and the Guide for the Care and Use of Laboratory Animals based on approved protocols by Houston Methodist Research Institute's Institutional Animal Care and Use Committees. APTES-modified nanoneedles (Supporting Information) were thoroughly cleaned with ethanol, dried under UV, and then loaded with 660 nm CdTe quantum dots (PlasmaChem GmbH). The solution was allowed to dry on the needles and then was immediately used for experiments.

The loaded nanoneedles were imprinted on the skin (back or ear) and muscle of male athymic nude mice (n = 3) (NCr-Fox1^{nu}; 4−6 weeks old). Animals were anesthetized and directly nanoinjected in the case of skin. For muscle, the superficial gluteal and lumbar muscles were exposed by surgical incision, gently elevating the fascia from the underlying muscle. The nanoneedles were inserted in direct contact with the lumbar and gluteal muscle on the right side. Nanoneedles were removed within 2 min from the insertion. Mice were imaged using a Xenogen IVIS200 housed within the preclinical imaging core facility at HMRI. Mice were imaged at predetermined times to study the release kinetics of quantum dots from the site of treatment. Data were quantified with Living Image 4.1.

Histology. Histological analysis for H&E and fluorescence imaging on muscle, skin, and ear was performed. Tissues were harvested and fixed in formalin prior to embedding into paraffin. Paraffin sections were then deparaffinized with xylene and rehydrated with decreasing concentrations of ethanol followed by washings in water. Staining occurred immediately

after this step either with H&E or with AF488 WGA and DAPI for fluorescence imaging of quantum dots and then coverslipped. Furthermore, unstained sections of tissues were used to quantify quantum dot fluorescence.

Conflict of Interest: The authors declare no competing financial interest.

Acknowledgment. The authors would like to acknowledge S. Amra from UTHSC for tissue paraffinization, sectioning, and H&E staining, K. Dunner Jr. for TEM sample preparation and analysis at the High-Resolution Electron Microscopy Facility at The University of Texas M.D. Anderson Cancer Center (UTMDACC), and HMRI Translational Imaging—PreClinical Imaging (Small Animal) Core for the use of IVIS200. This work was supported financially by the Defense Advanced Research Projects Agency (W911NF-11-0266), the Department of Defense (W81XWH-12-10414), the NIH (1R21CA173579-01A1), and UTMDACC Institutional Core Grant #CA16672; C.C. was supported by the Newton International Fellowship and the Marie Curie International Incoming Fellowship; J.O.M. was supported by a NIH predoctoral fellowship, 5F31CA154119-02. M.M.S. was supported by a Wellcome Trust Senior Investigator Award, EPSRC grant EP/K020641/1, and ERC consolidator grant "Naturale-CG". C.C. and M.M.S. would like to thank the Rosetrees Trust for financial support.

Supporting Information Available: Supplementary figures, movies, and extended material section are available free of charge *via* the Internet at http://pubs.acs.org.

REFERENCES AND NOTES

1. Shalek, A. K.; Gaublomme, J. T.; Wang, L.; Yosef, N.; Chevrier, N.; Andersen, M. S.; Robinson, J. T.; Pochet, N.; Neuberg, D.; Gertner, R. S.; *et al*. Nanowire-Mediated Delivery Enables Functional Interrogation of Primary Immune Cells: Application to the Analysis of Chronic Lymphocytic Leukemia. *Nano Lett.* **2012**, *12*, 6498–6504.
2. Han, S. W.; Nakamura, C.; Obataya, I.; Nakamura, N.; Miyake, J. A Molecular Delivery System by Using AFM and Nanoneedle. *Biosens. Bioelectron.* **2005**, *20*, 2120–2125.
3. Shalek, A. K.; Robinson, J. T.; Karp, E. S.; Lee, J. S.; Ahn, D. R.; Yoon, M. H.; Sutton, A.; Jorgolli, M.; Gertner, R. S.; Gujral, T. S.; *et al*. Vertical Silicon Nanowires as a Universal Platform for Delivering Biomolecules into Living Cells. *Proc. Natl. Acad. Sci. U.S.A.* **2010**, *107*, 1870–1875.
4. McKnight, T. E.; Melechko, A. V.; Hensley, D. K.; Mann, D. G. J.; Griffin, G. D.; Simpson, M. L. Tracking Gene Expression after DNA Delivery Using Spatially Indexed Nanofiber Arrays. *Nano Lett.* **2004**, *4*, 1213–1219.
5. Na, Y.-R.; Kim, S. Y.; Gaublomme, J. T.; Shalek, A. K.; Jorgolli, M.; Park, H.; Yang, E. G. Probing Enzymatic Activity Inside Living Cells Using a Nanowire—Cell "Sandwich" Assay. *Nano Lett.* **2013**, *13*, 153–158.
6. Chiappini, C.; De Rosa, E.; Martinez, J. O.; Liu, X.; Steele, J.; Stevens, M. M.; Tasciotti, E. Biodegradable Silicon Nanoneedles for the Intracellular Delivery of Nucleic Acids Induce Localized *in Vivo* Neovascularization. *Nat. Mater.* published ahead of print doi: 10.1038/NMAT4249.
7. Spira, M. E.; Hai, A. Multi-Electrode Array Technologies for Neuroscience and Cardiology. *Nat. Nanotechnol.* **2013**, *8*, 83–94.
8. Park, J.-H.; Gu, L.; von Maltzahn, G.; Ruoslahti, E.; Bhatia, S. N.; Sailor, M. J. Biodegradable Luminescent Porous Silicon Nanoparticles for *in Vivo* Applications. *Nat. Mater.* **2009**, *8*, 331–336.
9. Han, S. W.; Nakamura, C.; Kotobuki, N.; Obataya, I.; Ohgushi, H.; Nagamune, T.; Miyake, J. High-Efficiency DNA Injection into a Single Human Mesenchymal Stem Cell Using a Nanoneedle and Atomic Force Microscopy. *Nanomed. Nanotechnol. Biol. Med.* **2008**, *4*, 215–225.
10. Xu, A. M.; Aalipour, A.; Leal-Ortiz, S.; Mekhdjian, A. H.; Xie, X.; Dunn, A. R.; Garner, C. C.; Melosh, N. A. Quantification of Nanowire Penetration Into Living Cells. *Nat. Commun.* **2014**, *5*, 3614.
11. Robinson, J. T.; Jorgolli, M.; Shalek, A. K.; Yoon, M.-H.; Gertner, R. S.; Park, H. Vertical Nanowire Electrode Arrays as a Scalable Platform for Intracellular Interfacing to Neuronal Circuits. *Nat. Nanotechnol.* **2012**, *7*, 180–184.
12. Wang, Y.; Yang, Y.; Yan, L.; Kwok, S. Y.; Li, W.; Wang, Z.; Zhu, X.; Zhu, G.; Zhang, W.; Chen, X.; *et al*. Poking Cells for Efficient Vector-Free Intracellular Delivery. *Nat. Commun.* **2014**, *5*, 4466.
13. Obataya, I.; Nakamura, C.; Han, S.; Nakamura, N.; Miyake, J. Mechanical Sensing of the Penetration of Various Nanoneedles Into a Living Cell Using Atomic Force Microscopy. *Biosens. Bioelectron.* **2005**, *20*, 1652–1655.
14. Duan, X.; Gao, R.; Xie, P.; Cohen-Karni, T.; Qing, Q.; Choe, H. S.; Tian, B.; Jiang, X.; Lieber, C. M. Intracellular Recordings of Action Potentials by an Extracellular Nanoscale Field-Effect Transistor. *Nat. Nanotechnol* **2011**, *7*, 174–179.
15. Luxembourg, A.; Evans, C. F.; Hannaman, D. Electroporation-Based DNA Immunisation: Translation to the Clinic. *Expert Opin. Biol. Ther.* **2007**, *7*, 1647–1664.
16. Lefesvre, P.; Attema, J.; van Bekkum, D. A Comparison of Efficacy and Toxicity between Electroporation and Adenoviral Gene Transfer. *BMC Mol. Biol.* **2002**, *3*, 12.
17. Rostgaard, K. R.; Frederiksen, R. S.; Liu, Y.-C. C.; Berthing, T.; Madsen, M. H.; Holm, J.; Nygård, J.; Martinez, K. L. Vertical Nanowire Arrays as a Versatile Platform for Protein Detection and Analysis. *Nanoscale* **2013**, *5*, 10226–10235.
18. Yan, R.; Park, J.-H.; Choi, Y.; Heo, C.-J.; Yang, S.-M.; Lee, L. P.; Yang, P. Nanowire-Based Single-Cell Endoscopy. *Nat. Nanotechnol.* **2011**, *7*, 191–196.
19. Lacerda, L.; Bianco, A.; Prato, M.; Kostarelos, K. Carbon Nanotubes as Nanomedicines: From Toxicology to Pharmacology. *Adv. Drug Delivery Rev.* **2006**, *58*, 1460–1470.
20. Zhao, X.; Liu, R. Recent Progress and Perspectives on the Toxicity of Carbon Nanotubes at Organism, Organ, Cell, and Biomacromolecule Levels. *Environ. Int.* **2012**, *40*, 244–255.
21. Mitchell, L. A.; Gao, J.; Vander Wal, R.; Gigliotti, A.; Burchiel, S. W.; McDonald, J. D. Pulmonary and Systemic Immune Response to Inhaled Multiwalled Carbon Nanotubes. *Toxicol. Sci.* **2007**, *100*, 203–214.
22. Sato, Y.; Yokoyama, A.; Shibata, K.-I.; Akimoto, Y.; Ogino, S.-I.; Nodasaka, Y.; Kohgo, T.; Tamura, K.; Akasaka, T.; Uo, M.; *et al*. Influence of Length on Cytotoxicity of Multi-Walled Carbon Nanotubes Against Human Acute Monocytic Leukemia Cell Line THP-1 *in Vitro* and Subcutaneous Tissue of Rats *in Vivo*. *Mol. BioSyst.* **2005**, *1*, 176–182.
23. Nagai, H.; Okazaki, Y.; Chew, S. H.; Misawa, N.; Yamashita, Y.; Akatsuka, S.; Ishihara, T.; Yamashita, K.; Yoshikawa, Y.; Yasui, H.; *et al*. Diameter and Rigidity of Multiwalled Carbon Nanotubes Are Critical Factors in Mesothelial Injury and Carcinogenesis. *Proc. Natl. Acad. Sci. U.S.A.* **2011**, *108*, E1330–E1338.
24. Ge, C.; Du, J.; Zhao, L.; Wang, L.; Liu, Y.; Li, D.; Yang, Y.; Zhou, R.; Zhao, Y.; Chai, Z.; *et al*. Binding of Blood Proteins to Carbon Nanotubes Reduces Cytotoxicity. *Proc. Natl. Acad. Sci. U.S.A.* **2011**, *108*, 16968–16973.
25. Voskerician, G.; Shive, M. S.; Shawgo, R. S.; Recum, H. V.; Anderson, J. M.; Cima, M. J.; Langer, R. Biocompatibility and Biofouling of MEMS Drug Delivery Devices. *Biomaterials* **2003**, *24*, 1959–1967.
26. Weisenberg, B. A.; Mooradian, D. L. Hemocompatibility of Materials Used in Microelectromechanical Systems: Platelet Adhesion and Morphology *in Vitro*. *J. Biomed. Mater. Res.* **2002**, *60*, 283–291.
27. Polikov, V. S.; Tresco, P. A.; Reichert, W. M. Response of Brain Tissue to Chronically Implanted Neural Electrodes. *J. Neurosci. Meth.* **2005**, *148*, 1–18.
28. Anderson, S. H. C.; Elliott, H.; Wallis, D. J.; Canham, L. T.; Powell, J. J. Dissolution of Different Forms of Partially Porous Silicon Wafers under Simulated Physiological Conditions. *Phys. Status Solidi A* **2003**, *197*, 331–335.
29. Anglin, E.; Cheng, L.; Freeman, W.; Sailor, M. Porous Silicon in Drug Delivery Devices and Materials. *Adv. Drug Delivery Rev.* **2008**, *60*, 1266–1277.

30. Low, S. P.; Voelcker, N. H.; Canham, L. T.; Williams, K. A. The Biocompatibility of Porous Silicon in Tissues of the Eye. *Biomaterials* **2009**, *30*, 2873–2880.
31. Tasciotti, E.; Liu, X.; Bhavane, R.; Plant, K.; Leonard, A. D.; Price, B. K.; Cheng, M. M.-C.; Decuzzi, P.; Tour, J. M.; Robertson, F.; *et al*. Mesoporous Silicon Particles as a Multistage Delivery System for Imaging and Therapeutic Applications. *Nat. Nanotechnol.* **2008**, *3*, 151–157.
32. Tanaka, T.; Mangala, L. S.; Vivas-Mejia, P. E.; Nieves-Alicea, R.; Mann, A. P.; Mora, E.; Han, H. D.; Shahzad, M. M. K.; Liu, X.; Bhavane, R.; *et al*. Sustained Small Interfering RNA Delivery by Mesoporous Silicon Particles. *Cancer Res.* **2010**, *70*, 3687–3696.
33. Goh, A. S.-W.; Chung, A. Y.-F.; Lo, R. H.-G.; Lau, T.-N.; Yu, S. W.-K.; Chng, M.; Satchithanantham, S.; Loong, S. L.-E.; Ng, D. C.-E.; Lim, B.-C.; *et al*. A Novel Approach to Brachytherapy in Hepatocellular Carcinoma Using a Phosphorous32 (32P) Brachytherapy Delivery Device—a First-in-Man Study. *Int. J. Radiat. Oncol. Biol. Phys.* **2007**, *67*, 786–792.
34. Decuzzi, P.; Godin, B.; Tanaka, T.; Lee, S. Y.; Chiappini, C.; Liu, X.; Ferrari, M. Size and Shape Effects in the Biodistribution of Intravascularly Injected Particles. *J. Controlled Release* **2010**, *141*, 320–327.
35. Tanaka, T.; Godin, B.; Bhavane, R.; Nieves-Alicea, R.; Gu, J.; Liu, X.; Chiappini, C.; Fakhoury, J. R.; Amra, S.; Ewing, A. *In Vivo* Evaluation of Safety of Nanoporous Silicon Carriers Following Single and Multiple Dose Intravenous Administrations in Mice. *Int. J. Pharm.* **2010**, *402*, 190–197.
36. Ross, J. P.; Meenan, J.; Doherty, M. O.; Calara, J.; Palmer, D. H.; Heatley, S.; Chow, P. H. Novel Delivery via Endoscopic Ultrasound of a 32P Brachytherapy Device in Addition to Gemcitabine in Advanced Pancreatic Cancer. *ASCO Gastrointest. Cancer Symp.* **2008**, 25.
37. Xie, C.; Lin, Z.; Hanson, L.; Cui, Y.; Cui, B. Intracellular Recording of Action Potentials by Nanopillar Electroporation. *Nat. Nanotechnol.* **2012**, *7*, 185–190.
38. Hanson, L.; Lin, Z. C.; Xie, C.; Cui, Y.; Cui, B. Characterization of the Cell−Nanopillar Interface by Transmission Electron Microscopy. *Nano Lett.* **2012**, *12*, 5815–5820.
39. Xie, X.; Xu, A.; Angle, M. R.; Tayebi, N.; Verma, P.; Melosh, N. A. Mechanical Model of Vertical Nanowire Cell Penetration. *Nano Lett.* **2013**, 131115142023006.
40. Berthing, T.; Bonde, S.; Rostgaard, K. R.; Madsen, M. H.; Sørensen, C. B.; Nygård, J.; Martinez, K. L. Cell Membrane Conformation at Vertical Nanowire Array Interface Revealed by Fluorescence Imaging. *Nanotechnology* **2012**, *23*, 415102.
41. Bonde, S.; Berthing, T.; Madsen, M. H.; Andersen, T. K.; Buch-Månson, N.; Guo, L.; Li, X.; Badique, F.; Anselme, K.; Nygård, J.; *et al*. Tuning InAs Nanowire Density for HEK293 Cell Viability, Adhesion, and Morphology: Perspectives for Nanowire-Based Biosensors. *ACS Appl. Mater. Interfaces* **2013**, *5*, 10510–10519.
42. Wierzbicki, R.; Købler, C.; Jensen, M. R. B.; Łopacińska, J.; Schmidt, M. S.; Skolimowski, M.; Abeille, F.; Qvortrup, K.; Mølhave, K. Mapping the Complex Morphology of Cell Interactions with Nanowire Substrates Using FIB-SEM. *PLoS One* **2013**, *8*, e53307.
43. Chiappini, C.; Liu, X.; Fakhoury, J. R.; Ferrari, M. Biodegradable Porous Silicon Barcode Nanowires with Defined Geometry. *Adv. Funct. Mater.* **2010**, *20*, 2231–2239.
44. Chiappini, C.; Tasciotti, E.; Fakhoury, J. R.; Fine, D.; Pullan, L.; Wang, Y.-C.; Fu, L.; Liu, X.; Ferrari, M. Tailored Porous Silicon Microparticles: Fabrication and Properties. *ChemPhysChem* **2010**, *11*, 1029–1035.
45. Martinez, J. O.; Chiappini, C.; Ziemys, A.; Faust, A. M.; Kojic, M.; Liu, X.; Ferrari, M.; Tasciotti, E. Engineering Multi-Stage Nanovectors for Controlled Degradation and Tunable Release Kinetics. *Biomaterials* **2013**, *34*, 8469–8477.
46. Crichton, M. L.; Donose, B. C.; Chen, X.; Raphael, A. P.; Huang, H.; Kendall, M. A. F. The Viscoelastic, Hyperelastic and Scale Dependent Behaviour of Freshly Excised Individual Skin Layers. *Biomaterials* **2011**, *32*, 4670–4681.